COMMUNICATIONS MATERIALS

ARTICLE

https://doi.org/10.1038/s43246-020-00064-4 OPEN

Mechanistic study of superlattice-enabled high toughness and hardness in MoN/TaN coatings

Rainer Hahn[1✉], Nikola Koutná[1], Tomasz Wójcik[1], Anton Davydok[2], Szilárd Kolozsvári[3], Christina Krywka[2], David Holec[4], Matthias Bartosik[1] & Paul H. Mayrhofer[1]

Machining and forming tools exposed to challenging environments require protective coatings to extend their lifetime and reliability. Although transition metal nitrides possess excellent strength and resistance against chemical attacks, they lack ductility and are prone to premature failure. Here, by investigating structural and mechanical properties of MoN-TaN superlattices with different bilayer thickness, we develop coatings with high fracture toughness and hardness, stemming from the formation of a metastable tetragonally distorted phase of TaN up to layer thicknesses of 2.5 nm. Density functional theory calculations and experimental results further reveal a metal-vacancy stabilized cubic $Ta_{0.75}N$ phase with an increased Young's modulus but significantly lower fracture toughness. We further discuss the influence of coherency strains on the fracture properties of superlattice thin films. The close interplay between our experimental and ab initio data demonstrates the impact of phase formation and stabilization on the mechanical properties of MoN-TaN superlattices.

[1] Institute of Materials Science and Technology, TU Wien, 1060 Vienna, Austria. [2] Helmholtz-Zentrum Geesthacht - Zentrum für Material- und Küstenforschung GmbH, 21502 Geesthacht, Germany. [3] Plansee Composite Materials GmbH, 86983 Lechbruck am See, Germany. [4] Department of Materials Science, Montanuniversität Leoben, 8700 Leoben, Austria. ✉email: rainer.hahn@tuwien.ac.at

Thin ceramic films deposited using physical vapor deposition (PVD), i.e. transition metal borides, carbides, nitrides, and oxides, are used as protective coatings in the cutting and forming tool industry[1,2]. They prolong the lifetime of their underlying tool, e.g. WC–Co or hot working steel, by up to some 100%. Their beneficial properties like high hardness, high Young's modulus, chemical stability, thermal stability, and oxidation resistance provide an ideal basis for application in harsh environments[3–5]. However, the constant endeavor in industrial processes for increased throughput in cutting and forming processes without suffering restrictions in reliability leads to a demand for even better coatings. A weak point is typically their low fracture toughness K_{IC}, which is a material property difficult to quantify for hard coatings and thus has yet to be comprehensively researched. However, recent advances in micromechanical testing methods—applying in situ secondary electron microscope testing (SEM) using focused ion beam (FIB) shaped geometries—established the possibility to do so[6–9]. Since low K_{IC} values can lead to premature failure of the coating and thus to lack of performance in industrial processes, especially when mechanical loads dominate the wear behavior, fracture toughness is technologically highly relevant[2]. Not only the fracture toughness—a property describing the resistance of a material against crack propagation—but also the damage tolerance, a term including strength and fracture toughness, is important to prevent early failure.

Known mechanisms to increase the fracture toughness of ceramic materials are based on either intrinsic or extrinsic mechanisms[10]. While extrinsic mechanisms are often based on a reduction of the stress intensity at the crack tip, intrinsic effects draw upon increasing necessary maximum stress intensities for crack propagation as well as crack initiation. Examples for extrinsic strategies commercially used in hard coatings are for instance ductile phase toughening, toughening through nanostructural design, and toughening through multi- (nano-) layered structures[11–17]. Unlike that, intrinsic mechanisms are not easily accessible; however, Sangiovanni et al. calculated increased Poisson's ratio (ν), Cauchy pressure ($CP = c_{12}–c_{44}$), and decreased G/B ratio (all of the latter are indicating a more ductile behavior) for Mo, W, Nb, and Ta alloyed nitrides[18]. The authors propose that a toughness increase primarily originates from increased valence electron concentration (VEC) and the associated change in bonding states.

In this work, we combine two of the theoretically ductile nitrides, MoN and TaN, in a form of the superlattice architecture, i.e. alternating coherent MoN and TaN nanolayers. As indicated by our previous ab initio calculations, MoN/TaN superlattices outperform their monolithic MoN and TaN components in terms of B/G and Poisson's ratio. Consequently, even greater ductility than that of MoN and TaN (predicted by Sangiovanni[18] and by us[19]) can be achieved for MoN/TaN via the superlattice architecture. We envision—and confirm later in the manuscript—that additional advantage of the superlattice architecture is the improved fracture toughness, which can be enhanced up to 2.99 MPa $m^{1/2}$ by tuning the bilayer period. Our previous modeling and experimental results (XRD, EDX, nanoindentation) further suggest that only ~50% of N sites in MoN layers of MoN/TaN superlattices are occupied and that TaN is stabilized in a form of a tetragonally distorted zeta-phase[19] due to the template effect from $MoN_{0.5}$. This is a somewhat surprising finding which can not be simply deduced based on the knowledge of the monolithic MoN and TaN coatings. Vacancies play a critical role in a stabilization of the cubic (fcc, $Fm\bar{3}m$) phase. While MoN favors nitrogen vacancies (their specific content depends on the applied N_2 partial pressure and can reach up to 50%), TaN is stabilized by metal vacancies as $Ta_{0.75}N$ or by Schottky defects[20].

We identified MoN/TaN as a promising material system, however, it did not make any link between mechanical properties and the most important tuning parameter known for SL architectures: the bilayer period. The purpose of the present work is to investigate the fracture properties of $MoN_{0.5}$/TaN SL coatings with different bilayer periods. We expect that the combination of very similar shear modulus (124 GPa for the cubic $MoN_{0.5}$ and 127 GPa for cubic, defect-free TaN, and 159 GPa for ζ-TaN) but notably different structural parameters could lead to a strong superlattice effect mirrored by significant enhancement of fracture properties. Furthermore, this would enable us to provide new insight on the relevant mechanism behind the fracture toughness enhancement observed for superlattice films apart from the well-known hardness increase[21].

We demonstrate the structure–property relation of the MoN/TaN coating system by applying in situ micromechanical experiments, X-ray diffraction, scanning electron microscopy, transmission electron microscopy investigations and synchrotron nanodiffraction experiments. The latter experiments were performed to possibly verify the presence of ζ-TaN by probing small volumes, as well as to review the XRD data and perform residual stress measurements. The results are corroborated and supplemented using ab initio calculations together with a continuum mechanics model.

Results

Ab initio calculations. To estimate the relative tendency for brittle/ductile behavior of the monolithic as well as SL coatings, first-principles calculations on elastic constants were carried out. The structures in question were rs-$MoN_{0.5}$, rs-TaN, $MoN_{0.5}$/TaN SL with (001) interface, and $\Lambda = 1.7$ and 3.5 nm, as well as rs-AlN, rs-TiN, and AlN/TiN SL with (001) interface and $\Lambda = 1.7$ nm for comparison. The polycrystalline bulk, B, shear, G, and Young's moduli, E, together with the Poisson ratio, ν, and Cauchy pressure, CP, were evaluated using the calculated elastic constants. Subsequently, the brittleness/ductility map was constructed by plotting ν and CP/E, respectively, against the G/B ratio. Figure 1 clearly shows that all our data points fall onto the decreasing hyperbolic line connecting CP/E over B/G values of cubic and hexagonal structures. Unlike the rs-AlN, rs-TiN, and AlN/TiN SL, the rs-$MoN_{0.5}$, rs-TaN, $MoN_{0.5}$/TaN SL are found within the ductile region. The rs-TaN is predicted to slightly outperform its monolithic rs-$MoN_{0.5}$ counterpart in terms of ductility, whereas the behavior of $MoN_{0.5}$/TaN SL seems to be largely influenced by the bilayer period. Specifically, the SL with $\Lambda = 1.7$ nm is less ductile than its single-phase components, unlike the $\Lambda = 3.5$ nm variant, which leads to the highest ductility out of all the here considered structures.

The literature data presented in Fig. 1 show a hyperbolic relationship between the G/B and the CP/E ratio. The relation is described by ref. [22] as a universal criterion for cubic materials regarding their strength and ductility. Deviations from this relation mostly belong to metastable structures, i.e. rs-AlN or rs-TaN. Also, the data for hexagonal diborides (light gray stars in Fig. 1) fall on a hyperbola, located ~0.3 CP/E under that of cubic materials. This in turn would tell us that diborides, in general, tend to be stronger but less ductile in comparison with their cubic counterparts. Also, in this case, deviations from the hyperbola mostly belong to metastable structures.

Motivated by the ab initio predicted promising toughness and ductility of the MoN/TaN system, we proceeded with experimental investigations. As a first step, we employed electron microscopy and diffraction methods to study the morphology of the deposited MoN_x/TaN multilayered coatings.

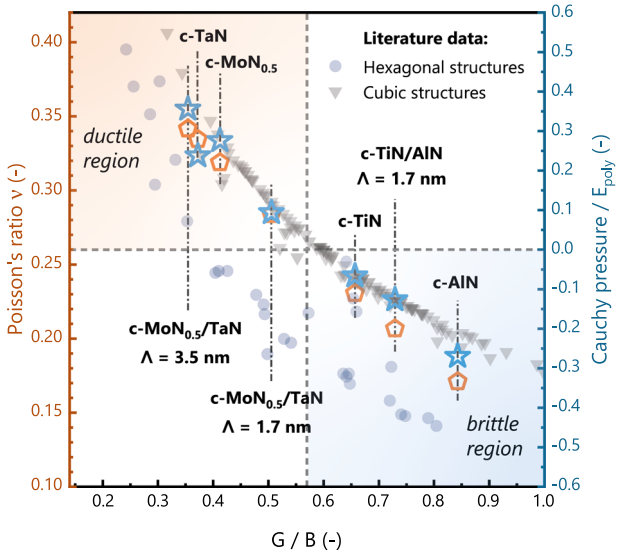

Fig. 1 Density functional theory studies describing the ductility. The Poisson's ratio (according to the Frantsevich's criterion: $\nu > 0.26$ for ductile materials[62]) as a function of the *G/B* ratio (according to Pugh's criterion, $G/B > 0.571$ for ductile materials[63]) is indicated by orange pentagons. The *G/B* dependence of the Cauchy pressure over the polycrystalline Young's modulus ($CP/E > 0$ for tough materials[64]) is indicated with blue stars, gray triangles for literature data of cubic structures and blue circles for literature data of hexagonal structures. Our calculations are labeled using dotted–dashed lines. The ductile region is located at the left top corner (orange background), the brittle region at the bottom right corner (blue background). The dashed lines mark the various toughness criteria (the scale was chosen in a way that Frantsevich's criterion and the criterion by Niu et al.[64] are on the same height). Exact values for literature data are given in Supplementary Table 1.

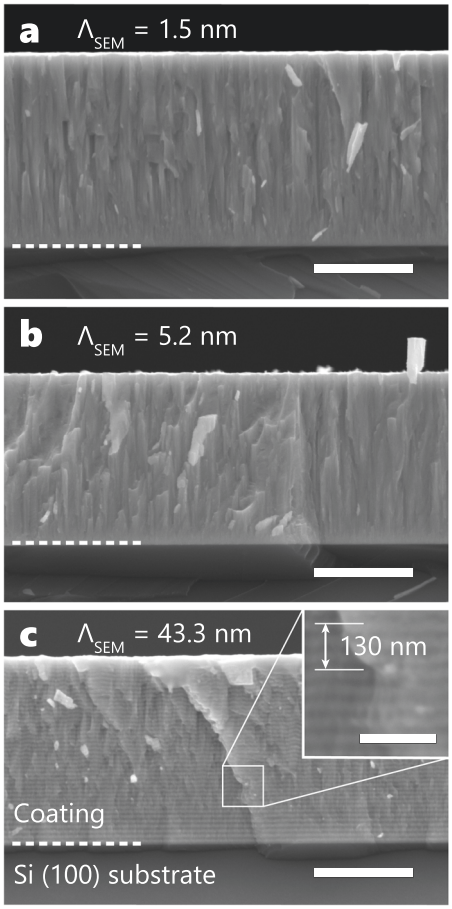

Fig. 2 Cross-sectional SEM studies. The SEM-micrographs in (**a–c**) show cross sections of our MoN–TaN coatings with nominal bilayer periods of 1.5, 5.2, and 43.3 nm, respectively. The dashed lines sign the interface between the coating and Si (100) substrate. The inset in (**c**) shows an enlarged view visualizing the layered structure of this coating. The scale bars in (**a**) to (**c**) are 1 µm, the scale bar in the inset has a length of 200 nm.

Structure and morphology. Our coatings have a dense morphology, visible in the SEM cross section pictures (Fig. 2a–c). We can further state that there was no interrupted growth as the columns are not re-nucleating between the single layers (inset in Fig. 2c), indicating a coherent growth.

This is also shown in Fig. 3a, c depicting TEM cross sections of the coatings with $\Lambda = 9.0$ and 3.0 nm, respectively. Additionally, we observe the desired layered structure; the bilayer periods of these samples were measured to be ~ 8.5 and 2.9 nm (by averaging 10 bilayers, not shown here). The white square in Fig. 3c shows the region chosen for Fast Fourier Transformation (FFT), Fig. 3f. We do not observe any sign of other phases than cubic structures in the [110] orientation.

A typical plan view TEM image is given in Fig. 3d ($\Lambda = 1.5$ nm). The in-plane grain size, i.e. the column width, of our coatings is $D_{||}$ ~ 46 nm as obtained by applying the linear intercept method[23]. The selected area electron diffraction (SAED) pattern of our TEM samples, Fig. 3b, e, shows no signs of other phases than cubic structured nitride (the main detectable orientations are labeled). To enhance the visibility of the structures present, we also integrated the SAED pattern using the PASAD plugin[24] of Gatan Digital Micrograph and subtracted the underground (inserted).

X-ray diffraction experiments show cubic structures in the measured out-of-plane direction (Bragg–Brentano). We do not observe any signs of the hexagonal TaN phase; also, Mo–N is present in its cubic $MoN_{0.5}$ structure following the accordance of measured, calculated, and literature-based lattice constants (2.101 Å and 2.090 Å for calculated and literature-based values, respectively) (Fig. 4a)[25,26]. The coatings with $\Lambda = 1.5$ and 3.0 nm show the main Bragg reflections (111) and (200) in between the calculated peak positions for ζ-TaN and $MoN_{0.5}$ (35.1° & 37.0°, and 40.7° & 43.0°, respectively). With an increasing bilayer period, these peaks split into two separate peaks each, staying at a similar position for larger Λ (Fig. 4a). Additionally, one can deduct from the XRD measurements a pronounced layered structure due to positive and negative satellite peaks (indicated with $m \pm 1$). The intensity of these satellites relative to the main peaks increases with increasing bilayer period (1.5–9.0 nm), suggesting an improving layer quality (definiteness) when assuming a constant inter-diffused zone (due to similar deposition conditions). The peaks in between both Bragg reflections for the sample with 9 nm bilayer period as well as those in between the peaks of $\Lambda = 15$ nm are assumed to be superlattice reflections. To confirm our adjusted nominal bilayer period, we evaluated the bilayer period using the following equation:

$$\sin\theta_{\pm} = \sin\theta_B \pm \frac{m \cdot \lambda}{2 \cdot \Lambda}, \quad (1)$$

where $\theta_{\pm}$ donates the diffraction angle of the satellite peak (positive or negative), θ_B the angle of the Bragg peak for the solid solution, m the order of the satellite peak, λ the wavelength of the used X-ray source and Λ the bilayer period. The results of these calculations given in Table 1 correlate well with the nominal

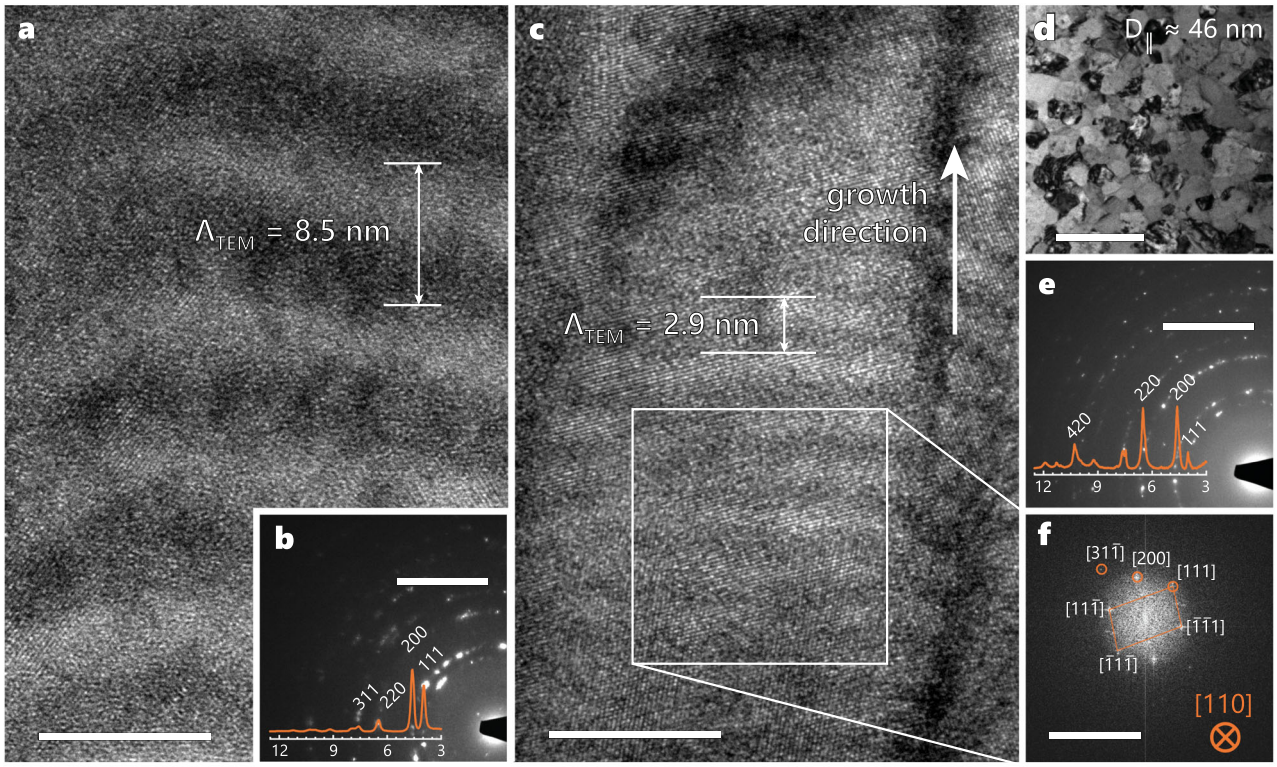

Fig. 3 TEM studies describing the microstructure. The HR-TEM micrographs (**a**) and (**c**) show a cross section of coatings with a nominal bilayer period of 9.0 and 3.0 nm, respectively. The white marked area in (**c**) was used to generate the FFT pattern in (**f**) calculated by Gatan Digital Micrograph. The TEM top view in (**d**) was taken from the sample with $\Lambda = 1.5$ nm, the column width was calculated using the linear intercept method. (**b**) and (**e**) show a SAED pattern of the region in (**a**) and (**d**), respectively, including an integration of the pattern. The scale bars in (**a**) and (**c**) are 10 nm, in (**b**) and (**e**) 5 nm^{-1}, in (**d**) 200 nm, and in (**f**) 10 nm^{-1}.

bilayer periods (also with those calculated by dividing the film thickness with the total number of bilayers).

Figure 4b shows a quarter of the Debye–Scherrer pattern of a $MoN_{0.5}$–TaN superlattice coating with a bilayer period of 5.2 nm grown on austenitic steel. The growth direction of this sample is towards $\varphi = 0°$. Therefore, the textured (200) nature of this sample can be identified, also indicated in the Bragg–Brentano high definition (BBHD) laboratory XRD measurements, Fig. 4a. In order to calculate the corresponding lattice constants in out-of-plane and in-plane directions, we integrated the intensity in the φ direction (Fig. 4c) and fitted these data (using Lorentz-peak shapes, see Fig. 4d). The corresponding lattice parameters vs. $\sin^2(\varphi)$ are linearly fitted and extrapolated to $\varphi = 0°$ and 90°. The coefficient of determination was $R^2 = 0.976$. We found a tetragonally distorted unit cell with a c/a ratio of 1.013. This distortion mostly originates from residual stresses, which are calculated to be −3.8 ± 0.2 GPa using the $\sin^2(\varphi)$ method; however, we also calculated a slight unit cell distortion (c/a ratio of 1.00022 for $\Lambda = 1.72$ nm) in our ab initio simulations stemming from the superlattice structure and its intrinsic residual stresses on the atomic scale.

These values, as well as the constants derived from nanodiffraction experiments and our BBHD measurements, are illustrated in Fig. 5a. Figure 5b shows the unit cell (disordered vacancies) of $MoN_{0.5}$/ζ-TaN with $\Lambda = 1.72$ nm. In Fig. 5a, it is visible that the lattice constants move towards the calculated constituent values with increasing bilayer period (5.2 nm). For larger bilayer periods we observe decreasing lattice constants, well coinciding with our calculations for different phases allowing for following bilayer-period-depending phase-evolution interpretation: with increasing bilayer period an epitaxial stabilization of ζ-TaN on $MoN_{0.5}$ becomes energetically less favorable. We propose that a different structural variant of TaN starts to form in TaN layers at the expense of ζ-TaN when the bilayer period exceeds some critical level. The possible candidates, $Ta_{0.75}N$ and $Ta_{0.875}N_{0.875}$, contain vacancies and Schottky defects (i.e. the same amount of vacancies on both Ta and N sublattice), respectively, and are the most stable variants of the cubic TaN. Importantly, both $Ta_{0.75}N$ and $Ta_{0.875}N_{0.875}$ exhibit a lattice parameter that results in a d^{200} value closely overlapping with the experimental one (2.1716 Å and 2.1950 Å for $Ta_{0.75}N$ and $Ta_{0.875}N_{0.875}$, respectively). Also, the parameters derived from the nanodiffraction experiments are consistent with our ab initio calculations.

Mechanical properties. The hardness and Young's modulus of our coatings are plotted in Fig. 6a, b. The indentation hardness is comparable to that of typical physical vapor deposited $Ti_{1-x}Al_xN$ (~ 28–32 GPa[27,28]) and shows no significant increase. This is due to the similar shear moduli of $MoN_{0.5}$ (ab initio calculated value of 124 GPa), ζ-TaN (159 GPa), and rs-TaN (127 GPa), as the hardness enhancement in superlattices is usually obtained by the hindrance of dislocation movement over the interface due to those differences[29]. The shear moduli of the defect-containing TaN depends on the defect type and concentration and is calculated to be 191 and 121 GPa for $Ta_{0.75}N$ (metal vacancies) and $Ta_{0.875}N_{0.875}$(Schottky defects), respectively.

A relatively large scatter of indentation moduli, from about 375 up to 430 GPa, is measured depending on the bilayer period. While the experimental records for the indentation moduli of the

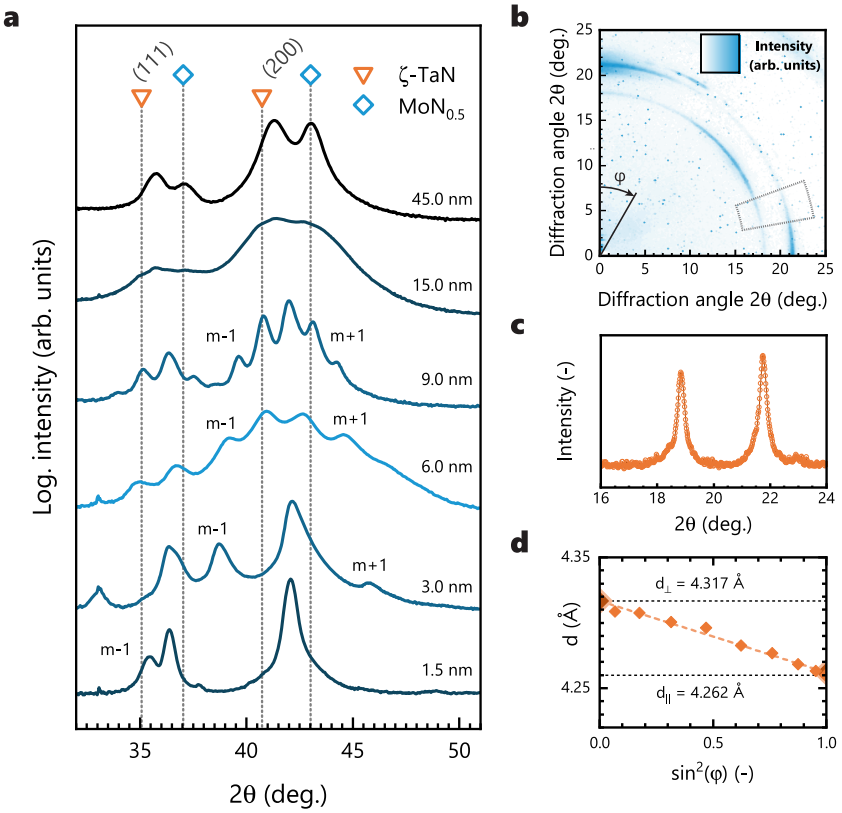

Fig. 4 X-ray diffraction analysis. X-ray diffraction patterns in (**a**) of our superlattice thin films. The labeling (m+1) and (m-1) mark the satellite peaks stemming from the layered structure of our coatings. The bilayer periods quoted on the right side of a are the nominal ones. The intensity plot in (**b**) shows a quarter of a Debye–Scherrer pattern recorded in transmission geometry (sample thickness in beam direction was ~50 μm) at the nanofocus endstation at the beamline P03 of PETRAIII at Deutsches Elektronen-Synchrotron (DESY). The gray marked area was integrated in φ direction and plotted in (**c**). The plot in (**d**) shows derived lattice parameters over $\sin^2(\varphi)$ and the corresponding linear fit.

Table 1 Nominal and measured bilayer periods.

Λ_{nom} (nm)	Λ_{SEM} (nm)	Λ_{XRD} (nm)	Λ_{TEM} (nm)
1.5	1.49±0.01	1.40±0.10	-
3.0	2.67±0.01	2.69±0.12	2.9
6.0	5.17±0.04	5.28±0.24	-
9.0	8.32±0.04	8.71±0.62	8.5
15.0	13.1±0.20	14.0±1.68	-
45.0	43.3±0.06	-	-

superlattices with bilayer periods above ~6 nm slowly saturate from 380 to about 400 GPa (the coating with Λ ~ 45 nm), they show an increase up to ~430 GPa when approaching $\Lambda = 1.7$ nm. To take a closer look at this peculiar dependence of our indentation data on the bilayer period, we applied the linear elasticity continuum model by Grimsditch and Nizzoli (cf. Methodology section). Our generalized version of this model allows us to calculate the overall elasticity of a SL containing material A and B based on the elastic contributions from the A/B interface layer and the bulk-like regions of the A and B layers. Furthermore, both A and B bulk-like layers can contain several sublayers with different concentrations of the respective material to consider, e.g., compositional fluctuations within one material. The bilayer period dependence enters via varying the volume ratio between the interface (of a certain thickness) and the bulk-like layers. Applied to our SL system, the $MoN_{0.5}$/TaN SL with $\Lambda = 1.7$ nm was used to model the interface layer, while the two bulk-like layers were approximated by rs-$MoN_{0.5}$ and tetragonally distorted ζ-TaN. Figure 6b reveals that under such assumptions, the indentation data for the samples with Λ in the 1.7–5 nm range can be very closely reproduced. However, the model deviates from the experimental records noticeably when the bilayer period exceeds 5 nm, hence suggesting possible structural transformations in one type of the layers (or both). Based on the dependence of the d_{200} spacings on the bilayer period, we proposed a hypothesis that the defect-containing rs-$Ta_{0.75}N$ or rs-$Ta_{0.875}N_{0.875}$ could form when the TaN layers become too thick to retain the defect-free ζ-TaN. Consequently, the material suspicious from structural transformations was the TaN, well known for its strong driving force for vacancies/Schottky defects. Specifically, the rs-$Ta_{0.75}N$ with 25% of ordered metal vacancies (illustrated as comic in Fig. 6c) is the energetically most favorable variant of the cubic TaN[26]. The TaN bulk-like layer of the SL in our Grimsditch–Nizzoli model was therefore divided into two sublayers containing ζ-TaN and (a) Schottky-defected $Ta_{0.875}N_{0.875}$ or (b) rs-$Ta_{0.75}N$. When the rs-$Ta_{0.75}N$ was implemented in the simulation, we obtained a close overlap between the indentation data and the calculated Young's moduli. Considerations of elastic response thus helped to differentiate between (energetically and structurally close) rs-$Ta_{0.75}N$ and rs-$Ta_{0.875}N_{0.875}$: we conclude that the presence of the former one in the SL is more likely. Therefore, the decrease of the indentation modulus was ascribed to the decreasing interface density as well as to the increasing volume fraction of ζ-TaN in the TaN layers. As the elasticity of the bulk-like region predominantly contributes to the overall elasticity of the SL at higher bilayer periods (i.e. the

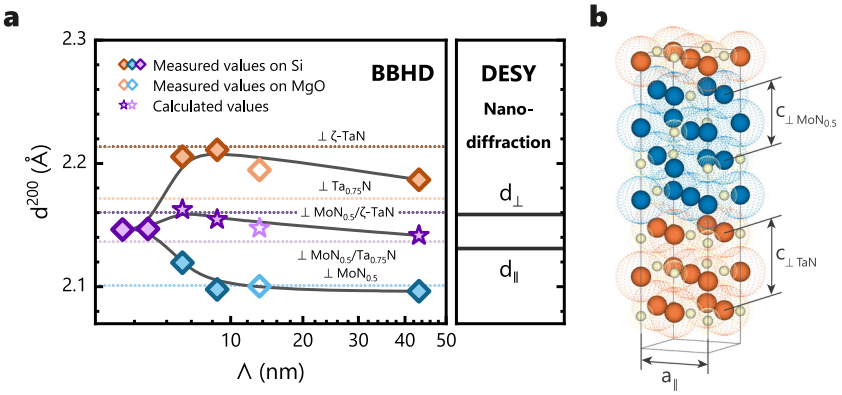

Fig. 5 Development of lattice parameter with increasing bilayer period. Diamond symbols in (**a**) show the obtained lattice plane distances from the XRD patterns of our superlattices on Si (100), Fig. 4a. The out-of-plane d^{200} lattice planes for ζ-TaN, $Ta_{0.75}N$, $MoN_{0.5}$, $MoN_{0.5}$/ ζ-TaN, and $MoN_{0.5}/Ta_{0.75}N$ are indicated with horizontal lines in (**a**). The results for the coating with $\Lambda = 13.1$ nm are obtained from films grown on MgO, as their the 200 XRD peak was more distinct (compare Fig. 4 and Supplementary Fig. S1). Data points in stars are obtained by calculating the average. The right side of a shows in-plane and out-of-plane lattice plane distances obtained from our synchrotron experiments. In (**b**) the unit cell of the superlattice with $\Lambda = 1.72$ nm is shown.

interface effects are largely diminished), this leads to the saturation of the indentation modulus towards the average polycrystalline Young's modulus of rs-$MoN_{0.5}$ and rs-$Ta_{0.75}N$.

The micromechanical testing setup with necessary dimensions used to calculate the fracture toughness is exemplarily shown in Fig. 6d. We gave special attention to the positioning of the spherical indenter tip to avoid deviations from mode I load conditions. Figure 6e, f shows fracture cross sections of cantilevers after testing. The thin material bridges are visible, as well as the initial notch depth a. The spherical indenter tip accompanies with a reduction of the lever arm l during the micromechanical test. The resulting overall error due to this uncertainty is calculated to be less than 2% (calculated in the framework of Euler–Bernoulli beam theory, also accounting for uncertainties coming with a blunted tip) and is already included in the experimental error. This is justified since a sharp indenter (i.e. Berkovich or cube corner) could lead to unwanted plastic deformation in the contact area, falsifying the outcome by incorrect displacement data, as well as by violations in mode I conditions due to forces in the lateral direction (inducing yield stresses in the cross section).

The derived fracture toughness K_{IC} of our MoN/TaN superlattice coatings (Fig. 6g) reaches a maximum value of 2.97 ± 0.21 MPa $m^{½}$ at a bilayer period of $\Lambda = 5.2$ nm. Compared to TiN/CrN superlattices, we observe higher fracture toughness values (there the maximum was 2.01 ± 0.18 MPa $m^{½}$ at a bilayer period of ~6.2 nm)[17]. The Ti–Si–N system reaches a maximum fracture toughness of ~ 3.0 ± 0.2 MPa $m^{½}$[15], and also for Ti–Al–N a K_{IC} of ~ 3.0 MPa $m^{½}$ can be achieved after annealing at 900 °C[12].

With increasing bilayer period, we observe a decrease in fracture toughness to 2.32 ± 0.23 MPa $m^{½}$ for 8.3 nm, when Λ is further increased, K_{IC} stays constant at ~ 2.5 MPa $m^{½}$. For decreasing bilayer periods ($\Lambda = 1.5$ nm) we see a decrease to 2.30 ± 0.13 MPa $m^{½}$. Although this behavior (superlattice effect on K_{IC}) has been reported in previous works on superlattices, the here presented K_{IC} peak for a certain bilayer period is observed without significant differences in the shear moduli of the constituents and hence, with no substantial hardness increase.

The H/E ratio (Fig. 6h), an empirical indication used to describe the toughness of hard coatings also shows an increase for bilayer periods between 3 and 6 nm. However, it has to be noted that the error bars are overlapping, thus these differences are not significant[30].

To provide an insight into the K_{IC} dependence on the bilayer period, we performed ab initio calculations quantifying cleavage properties of $MoN_{0.5}$/TaN SL as well as of the monolithic rs-$MoN_{0.5}$, ζ-TaN, and rs-$Ta_{0.75}N$, which were predicted to form in the bulk-like layers of the SL. Specifically, we determined cleavage energy, E_c, which represents the energy to separate a solid material into two blocks, and critical stress, σ_c, which corresponds to the maximum tensile stress perpendicular to the cleavage plane before cleavage happens[31]. In accordance with the experimental procedure, our SLs were cleaved perpendicularly to the interfaces. Subsequently, theoretical K_{IC}^* values were estimated using a simple formula

$$K_{IC}^* = \sqrt{c \cdot E_{hkl} \cdot E_C}, \quad (2)$$

where E_{hkl} and E_c are the directional Young's modulus and the cleavage energy, respectively, and c is a scaling factor, conventionally set to 4[32]. Table 2 shows that the E_{100} value of the $MoN_{0.5}$/TaN SL, i.e. Young's modulus perpendicular to the interface, is 618 GPa, which is close to the 645 and 671 GPa of ζ-TaN and rs-$TaN_{0.75}$, respectively, but way above the ~389 GPa for rs-$MoN_{0.5}$. The cleavage stresses as well as cleavage energies vary quite significantly between 32.6 GPa (SL) and 44.4 GPa (ζ-TaN) and 3.6 J/m^2 (SL) and 5.4 J/m^2 (ζ-TaN), respectively. According to the predicted K_{IC}^* values, crack propagation is the easiest in $MoN_{0.5}$ yielding K_{IC}^* ~2.59 MPa $m^{½}$. The K_{IC}^* of ~2.99 MPa $m^{½}$ for the 1.72 nm $MoN_{0.5}$/TaN SL suggests more for a rule-of-mixture-like behavior, as the K_{IC}^* values of ζ-TaN and rs-$Ta_{0.75}N$ are much higher with 3.72 and 3.25 MPa $m^{½}$, Table 2. Consequently, based on these DFT calculations the ζ-TaN phase provides the highest cleavage stresses and energies as well as highest K_{IC}^*.

Discussion

Using ab initio calculations to predict material properties has been proven to serve as a powerful tool in materials science. The theoretically calculated indicators for ductility (G/B, CP, and ν) and their comparison with literature values clearly indicate a trend towards increased ductility for $MoN_{0.5}$/TaN superlattice coatings. This also holds true compared to its constituents (Fig. 1). Furthermore, we identified ζ-TaN, $Ta_{0.75}N$, and rs-$MoN_{0.5}$ as the strongest constituents within our MoN–TaN superlattice system, in terms of cleavage stress and energy. Among these constituents, the calculated

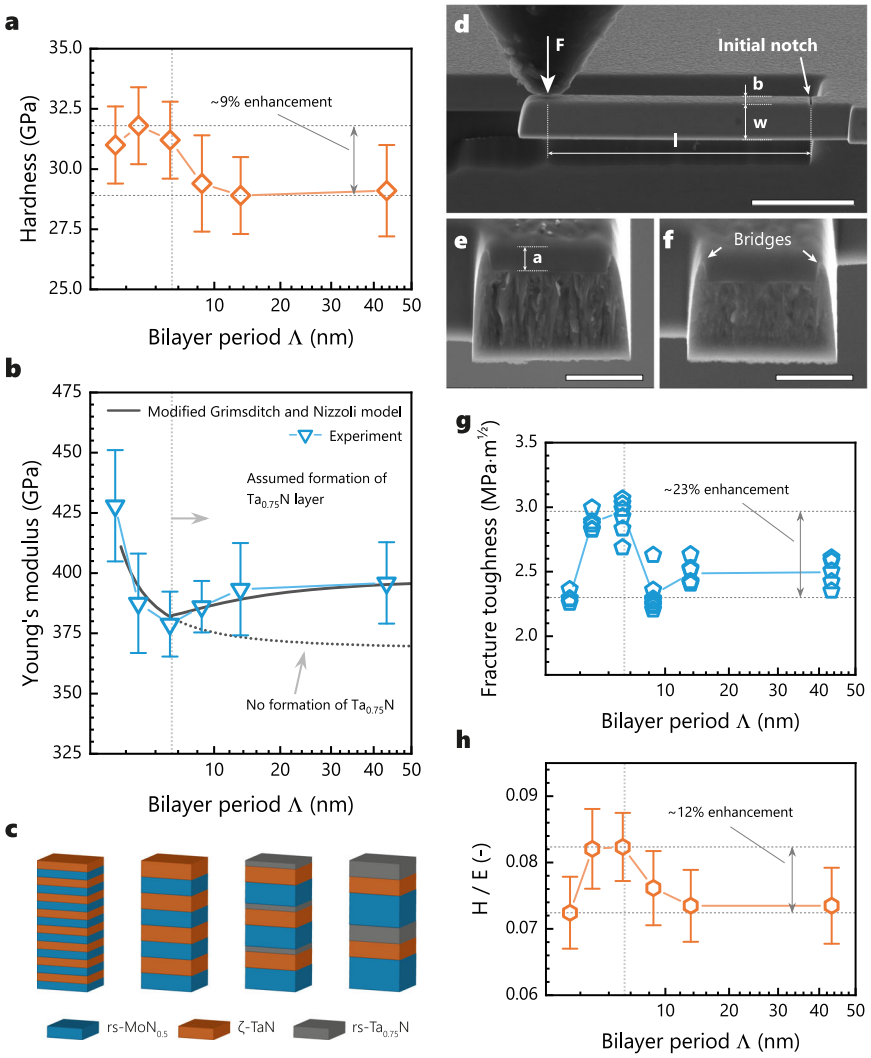

Fig. 6 The mechanical properties of MoN-TaN superlattice thin films. The hardness as a function of the bilayer period is shown in (**a**). The vertical dashed line indicates the bilayer period where we assume the formation of a second phase in the TaN layer. Young's modulus over Λ is shown in (**b**). Here, besides the computational Young's modulus (Grimsditch and Nizzoli) including a second phase in TaN, we also plotted the one without it. The sketch in (**c**) shows the proposed coating architecture. The SEM micrograph (**d**) shows a cantilever before micromechanical testing in a 10° inclined view including the dimensions of the lever arm *l*, cantilever width *b*, cantilever height *w*, the initial notch, and the point of application of force. The fracture cross sections in (**e**) (1.5 nm) and (f) (8.3 nm) show the depth of the initial notch *a*; exemplary marked are the thin bridges necessary for our micromechanical tests. The plots (**g**) and (**h**) show the derived fracture toughness K_{IC} and the empirical *H/E* toughness criteria, respectively. All mechanical properties were determined on sample deposited on Si (100), additionally, Young's modulus was cross-checked by performing nanoindentation experiments also on MgO (100), sapphire, and austenitic steel. All error bars represent standard deviation. The scale bar in (**d**) is 5 µm long, in (**e**), and (**f**) the scale bar is 1 µm long.

Table 2 Elastic properties and cleavage properties of the constituents of our superlattices as well as of the superlattice with a bilayer period of 1.72 nm.

Structure	Elastic properties (GPa)					Cleavage properties		
	B	*G*	E_{poly}	E_{100}	E_{111}	E_c (J/m^2)	σ_c (GPa)	K_{IC}^* (MPa m$^{1/2}$)
rs-$MoN_{0.5}$	300	124	326	399	284	4.0	34.6	2.59
rs-TaN	340	127	338	674	190	3.1	27.6	2.90
ζ-TaN	283	156	396	674	319	5.4	44.4	3.72
rs-$Ta_{0.75}N$	317	191	479	671	374	3.9	34.6	3.25
rs-$Ta_{0.875}N_{0.875}$	299	121	319	387	279	3.7	32.9	2.40
SL 1.7 nm	316	160	411	618	330	3.6	32.6	2.99

We note that the cleavage properties of the non-cubic (e.g., ζ-TaN) and the defected systems can generally fluctuate depending on the chosen cleavage plane. In accordance with the SL systems, which were cleaved perpendicularly to the interface, the ζ-TaN, was cleaved along the tetragonal *c* axis. Cleavage data for the cubic but defected systems were averaged based on the results for the distinct cleavage planes in our simulation cell.

K_{IC}* is with 3.72 MPa m$^{1/2}$ significantly higher for ζ-TaN than for any other phase or the $MoN_{0.5}$/TaN SL studied here. As we have recently proposed, this ζ-TaN phase, however, is only accessible for certain bilayer periods in the MoN–TaN SL system[19]. Therefore, we developed various $MoN_{0.5}$/TaN superlattice coatings with different bilayer periods. By comparing our experimentally obtained data (from detailed XRD and TEM studies) with calculated lattice constants and elastic constants as well as energy-of-formation studies of various MoN/TaN superlattices[19], we were able to draw the most realistic scenario of layer and phase arrangements, Fig. 6c, where an epitaxially (to $MoN_{0.5}$) stabilized tetragonal distorted ζ-TaN layer (up to ~2.5 nm layer thickness) leads the formation of an rs-$Ta_{0.75}N$ layer.

We do not observe strong intermixing—conceivable through diffusion processes—at the interfaces of our superlattice constituents. This is recognizable by the multiple satellite reflections in their XRD patterns, even for a nominal bilayer period of only 1.5 nm. Besides this, our TEM micrographs show curved interfaces stemming from kinetic limitations during the growth, as described in refs. [33,34]. The lattice parameters of the Mo–N-layers best match those calculated for $MoN_{0.5}$, d_{200} for the Ta-N layers gradually decrease from the value for ζ-TaN to $Ta_{0.75}N$ with increasing bilayer period (from ~ 5.2 nm to 45 nm) as shown in Fig. 5a. For superlattices with Λ = 1.5 and 3.0 nm, we observed just one XRD main peak in the out-of-plane direction, suggesting for strained unit cells due to lattice mismatch.

Typically, such conditions are the prerequisites for achieving high hardness-peaks, being easily above the hardness of the constituting materials. However, due to the relatively similar shear moduli of the two materials ($MoN_{0.5}$ and ζ-TaN), we do not observe a significant hardness-peak. Importantly though, we observe a clear peak in fracture toughness. Consequently, there need to be additional mechanisms active. In ref. [17], we studied the fracture toughness as well as the hardness of TiN/CrN SL films and found a pronounced dependence of both properties (K_{IC} and H) as a function of the bilayer period, having their peak-values at comparable bilayer periods. We proposed several mechanisms like (1) coherency strains, (2) misfit dislocation arrays at the interfaces, (3) spatially oscillating elastic moduli, and (4) average grain size, that can explain this behavior.

The MoN/TaN SL system studied here is an interesting model system as it essentially allows us to study the effect of largely different lattice parameters at comparably similar shear moduli (the difference in G is below 32 GPa). For comparison, ΔG for other well-studied SL systems is easily between ~50 and 90 GPa[17,35–37]. The average grain size of our MoN/TaN superlattices also shows no strong dependence on the bilayer period, contrary to other material combinations. The lattice mismatch of ~5% can result in residual stresses being comparably high to growth-related or thermal expansion related stresses. The lattice parameter difference of Δa = 0.225 Å (between $MoN_{0.5}$ and ζ-TaN), and an interface width of one unit cell (4 planes of each, nitrogen and metal, and thus five transitions with a change in lattice parameter) a total difference of 0.045 Å, results in coherency strains ε_c of ~1%. This gives residual stresses of ~3.3 GPa, both tensile and compressive surrounding the interfaces between $MoN_{0.5}$ and ζ-TaN. These stresses have to be overcome during cleavage, thus they effectively enhance the measured fracture toughness. This mechanism is illustrated in Fig. 7. Thereby, also the hardness slightly peaks as reported by Shinn and Barnett[38] and obtained for our samples. An additional mechanism increasing the fracture toughness without significantly influencing the hardness (as obtained for our samples) is suggested in our DFT calculations.

The peak of the experimental K_{IC} at a bilayer period of about 5 nm can partially be interpreted via compositional and structural changes within the TaN layers, being triggered by the superlattice arrangement with rs-$MoN_{0.5}$. The calculated K_{IC}* value has a maximum of ~3.72 MPa m^{½} for ζ-TaN. Hence, these superlattices that allow for the highest volume fraction of ζ-TaN will also provide a high K_{IC}. As the ζ-TaN phase is stabilized by the coherency strains to $MoN_{0.5}$[19] and from a certain TaN layer thickness onwards, the rs-structure will form, there is a close relationship with the bilayer period. This can also explain the decline of K_{IC} for bilayer periods above ~5 nm, as thereby the volume fraction of ζ-TaN decreases at the expense of the rs-TaN_x phase. The latter has a lower K_{IC}*, e.g., we calculated ~3.25 MPa m^{½} for rs-$TaN_{0.75}$. The real picture, of course, is much more complex, meaning that the ζ-phase formation is only one possible contributing factor to the observed K_{IC} evolution besides the bilayer period-depending coherency stresses.

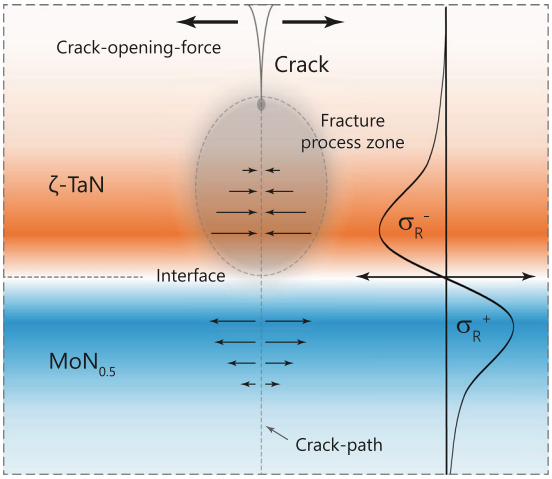

Fig. 7 Illustration of a fracture process in superlattice thin films. Schematics of the coherency strains and their consequential stresses influencing crack propagation across the interface. Here, the compressive residual stresses, pictured by arrows in the fracture process zone, impede crack growth across the interface.

To conclude, the concept of enhanced mechanical properties due to superlattice architectures has been shown in multiple studies. Together with increased hardness, the fracture toughness of protective coatings is of particular importance. We deposited MoN/TaN superlattice coatings, characterized them using density functional theory calculations, X-ray diffraction, and mechanical testing, coming to the following conclusion: the constituents of the MoN/TaN superlattice system are—when deposited by physical vapor deposition—present in the $MoN_{0.5}$ and ζ-TaN, $Ta_{0.75}N$, phases. The latter depends on individual layer thickness: we observe a change at a layer thickness of ~2.5 nm TaN. This was observed by two different methods: first, our XRD measurements confirm this trend as the peak position of the TaN layer shifts to higher 2θ angles with increasing bilayer periods as a result of increasing $Ta_{0.75}N$ proportion. Second, the progression of Young's modulus follows a calculation including the $Ta_{0.75}N$ phases after an initial growth of ~2.5 nm ζ-TaN instead of the calculation without it. We calculated an intrinsic higher fracture toughness for ζ-TaN compared to $Ta_{0.75}N$ as a part of an increase in K_{IC}. Another mechanism active in this superlattice coatings is coherency stresses which have to be overcome. This increase in K_{IC} was also observed in micromechanical experiments.

Methods

Coating deposition. Our coatings were deposited using a lab-scale AJA Orion 5 sputtering system. Two confocal 2-inch cathodes, equipped with an unbalanced magnetron system were powered in current-controlled mode at a maximum

current density of 19.7 mA/cm^2. Our targets had a purity of 99.6% (Plansee Composite Materials GmbH). The nanolayer architectures were realized using a computer-controlled shutter system. The base pressure of our coating system was lower than 10^{-4} Pa. Prior to deposition, the substrates were ultrasonically cleaned in acetone and ethanol for five minutes each, heated to deposition temperature (380 °C at the substrate), thermally cleaned for 20 min and plasma etched in Ar plasma (6 Pa). We used a gas mixture of Ar and N_2, 7 and 3 sccm, respectively, at a total pressure of 0.4 Pa to deposit our thin films on the rotating substrates (Si (100), MgO (100), Al_2O_3 ($1\bar{1}02$)). Austenitic steel was used as it has a polycrystalline nature and hence avoids an overexposing of synchrotron radiation on the detector. The nominal bilayer periods were set to 1.5, 3.0, 6.0, 9.0, 15.0, and 45.0 nm. Additionally—to achieve a dense coating morphology—we applied a negative bias voltage of −40 V.

Computational details. To carry out DFT calculations, we used the Vienna Ab-initio Simulation Package (VASP)[39,40] together with the projector augmented plane wave (PAW) pseudopotentials. The exchange-correlation effects were incorporated employing the generalized gradient approximation (GGA)[41] using a Perdew–Burke–Ernzerhof (PBE) exchange and correlation functional[42]. The plane-wave cut-off energy was always set to 600 eV, while the k-vector sampling (25000 k-points) of the Brillouin zone provided a total energy accuracy of about 10^{-3} eV/at.

The models for MoN/TaN superlattices were based on the cubic rock salt ($Fm\bar{3}m$) structure. Various bilayer periods were constructed by stacking the desired number of cubic cells in the (100) direction. Various defected states (vacancies or Schottky defects) were generated in an ordered or disordered manner employing the SQS method[43]. In the latter case, a sufficiently large supercell (containing 64 and 128 atoms for the bulk and the SL systems, respectively) was produced. Lattice parameters of the defect-free structures were optimized by fitting the energy vs. volume data with the Birch–Murnaghan equation of state[44], while all structure optimizations in the vacancy-containing supercells were performed by relaxing the volume, shape, and atomic positions.

To provide an insight into the elastic behavior of selected systems, a tensor of elastic constants was derived from Hooke's law by applying the stress-strain method[45–47]. Subsequently, we used the Voigt's notation to transform this fourth-order elastic tensor to a 6 × 6 matrix, which was further projected onto a desirable (cubic or tetragonal) symmetry[48]. The polycrystalline bulk, B, and shear, G, moduli were determined by averaging the Reuss's and Voigt's estimates[49,50], while the polycrystalline Young's modulus, E, was evaluated as

$$E = \frac{9 \cdot BG}{3 \cdot B + G} \tag{3}$$

Following formulae in ref. [51], we computed Young's modulus values in the prominent crystallographic directions. The tendency for brittle/ductile behavior was estimated by plotting the G/B ratio vs. Poisson's ratio, ν=(3B-2G)/(6B+2G), or Cauchy pressure/E, c_{12}–c_{44}/E. Considering the defected SLs—which do not exhibit overall cubic but tetragonal symmetry— as well as the hexagonal boride systems, effective Cauchy pressure value was estimated as $1/3(c_{12}-c_{66} + c_{13}-c_{55} + c_{23}-c_{44})$. Since bilayer-period-dependent trends in mechanical properties are very costly to obtain from first-principles (especially when it comes to defected systems), the increasing demands on CPU time and/or memory motivated us to estimate elastic properties of SLs with higher bilayer periods using a computationally cheaper approach by Grimsditch and Nizzoli[52]. In the original formulation, this linear elasticity continuum model allows us to calculate effective elastic constants of a system composed of two layers having arbitrary symmetry requiring elastic constants of the two-layer materials together with their volume ratio. The model, however, disregards any heterogeneity introduced by interfaces. In particular, the input elastic constants correspond to the equilibrium lattice parameters of each individual phase, which do not properly represent the stress state of the material in the SL. To provide a more realistic picture of the interface, the original formalism was extended to a generally n layers forming the SL in question[35]. The interface effects were modeled by setting the elastic constants of one of the n layer materials to those of a chosen superlattice with a small bilayer period. By varying the volume ratio of the interface layer (of a certain thickness) and the remaining bulk-like layers, we managed to predict elastic data depending on the desired bilayer period, which would not have been possible using the original Grimsditch–Nizzoli formalism. Furthermore, to corroborate our fracture experiments, the tensile strength in terms of cleavage energy and stress for brittle cleavage was estimated using the rigid-block displacement method[53,54].

Structural characterization. Transmission electron microscopy (TEM) investigations were performed on an FEI Tecnai F20 equipped with a field emission gun. All our TEM samples were produced using a dual beam FIB and applying the lift-out method[55]. To reduce the Ga^+ ion damage, we reduced the milling current down to 0.1 nA and sputter-cleaned our sample using a Technoorg Linda Gentlemill. X-ray diffraction patterns were recorded using a Panalytical XPert Pro MPD θ–θ diffractometer in Bragg–Brentano configuration. The x-ray source was a Cu-K_α source (λ = 1.5418 Å). Nanodiffraction experiments were conducted at the nanofocus endstation of Beamline P03 at PETRAIII located at synchrotron facility DESY (Hamburg), the used monochromatic X-ray radiation had a wavelength of λ = 0.80533 Å (15.0 keV beam energy). The sample was placed in transmission geometry, to collect Debye Scherrer patterns using a cross-sectional approach[56].

Mechanical properties. Hardness measurements were performed in compliance with guidelines given by ref. [57], and evaluated using the method after Oliver and Pharr with a Fischer Cripps Laboratories ultra-micro indentation system (UMIS) equipped with a Berkovich diamond tip[58]. To eliminate possible substrate effects, we calculated Young's modulus of our coatings by extrapolating E vs. h to zero indentation depth for different substrates following[59].

We conducted micromechanical experiments to calculate the fracture toughness of our thin films. Hereby, we first dissolved the substrate (Si (100)) in aqueous KOH (with a concentration of 40 wt.% KOH and a temperature of 70 °C) to obtain free-standing thin film material. We FIB machined microcantilevers (FEI Quanta 200 3D DBFIB) according to regulations given by[60]. The initial current used for milling with our Ga^+ ion source was 1.0 nA, subsequently reduced to 0.5 nA to prevent unwanted damage. The initial notch was machined with a current of 50 pA. These cantilevers were then loaded with a Hysitron PI-85 Scanning electron microscope (SEM) PicoIndenter equipped with a spherical diamond tip (diameter of 1 µm) inside an FEI Quanta 200 FEGSEM. We performed these tests in displacement-controlled mode (5 nm s^{-1}) to obtain the maximum force before failure. This also enabled us to monitor possible mode I violations and assure linear elastic behavior of our beams. The fracture toughness was then calculated according to Matoy et al.[61]:

$$K_{IC} = \frac{P_{max} \cdot l}{b \cdot w^{\frac{3}{2}}} \cdot f\left(\frac{a}{w}\right) \tag{4}$$

with

$$f\left(\frac{a}{w}\right) = 1.46 + 24.36 \cdot \left(\frac{a}{w}\right) - 47.21 \cdot \left(\frac{a}{w}\right)^2 + 75.18 \cdot \left(\frac{a}{w}\right)^3, \tag{5}$$

where P_{max} is the maximum force before fracture, a the depth of the initial notch, b the cantilever width, and w the cantilever thickness (film thickness in this case). We performed seven fracture tests for each system with a total success rate of 87%.

Data availability

The data that support the findings of this study are available from the authors on reasonable request.

Received: 19 February 2020; Accepted: 27 July 2020;
Published online: 18 August 2020

References

1. Mayrhofer, P. H., Mitterer, C., Hultman, L. & Clemens, H. Microstructural design of hard coatings. *Prog. Mater. Sci.* **51**, 1032–1114 (2006).
2. Inspektor, A. & Salvador, P. A. Architecture of PVD coatings for metalcutting applications: a review. *Surf. Coat. Technol.* **257**, 138–153 (2014).
3. Glechner, T. et al. Tuning structure and mechanical properties of Ta-C coatings by N-alloying and vacancy population. *Sci. Rep.* **8**, 17669 (2018).
4. Moraes, V. et al. Substoichiometry and tantalum dependent thermal stability of α-structured W-Ta-B thin films. *Scr. Mater.* **155**, 5–10 (2018).
5. Xu, Y. X. et al. Thermal stability and oxidation resistance of sputtered TiAlCrN hard coatings. *Surf. Coat. Technol.* **324**, 48–56 (2017).
6. Dehm, G., Jaya, B. N., Raghavan, R. & Kirchlechner, C. Overview on micro- and nanomechanical testing: New insights in interface plasticity and fracture at small length scales. *Acta Mater.* **142**, 248–282 (2018).
7. Jaya, B. N., Kirchlechner, C. & Dehm, G. Can microscale fracture tests provide reliable fracture toughness values? A case study in silicon. *J. Mater. Res.* **30**, 686–698 (2015).
8. Ast, J. et al. A review of experimental approaches to fracture toughness evaluation at the micro-scale. *Mater. Des.* **173**, 107762 (2019).
9. Pippan, R., Wurster, S. & Kiener, D. Fracture mechanics of micro samples: fundamental considerations. *Mater. Des.* **159**, 252–267 (2018).
10. Lawn, B. *Fracture of Brittle Solids* (Cambridge University Press, 1993).
11. Zhang, S., Sun, D., Fu, Y. & Du, H. Toughening of hard nanostructural thin films: a critical review. *Surf. Coat. Technol* **198**, 2–8 (2005).
12. Bartosik, M., Rumeau, C., Hahn, R., Zhang, Z. L. & Mayrhofer, P. H. Fracture toughness and structural evolution in the TiAlN system upon annealing. *Sci. Rep* **7**, 16476 (2017).
13. Hahn, R., Bartosik, M., Arndt, M., Polcik, P. & Mayrhofer, P. H. Annealing effect on the fracture toughness of CrN/TiN superlattices. *Int. J. Refract. Met. Hard Mater.* **71**, 352–356 (2018).
14. Fuger, C. et al. Influence of tantalum on phase stability and mechanical properties of WB $_2$. *MRS Commun.* **9**, 375–380 (2019).
15. Bartosik, M. et al. Fracture toughness of Ti–Si–N thin films. *Int. J. Refract. Met. Hard Mater.* **72**, 78–82 (2018).

16. Daniel, R. et al. Fracture toughness enhancement of brittle nanostructured materials by spatial heterogeneity: a micromechanical proof for CrN/Cr and TiN/SiOx multilayers. *Mater. Des.* **104**, 227–234 (2016).
17. Hahn, R. et al. Superlattice effect for enhanced fracture toughness of hard coatings. *Scr. Mater.* **124**, 67–70 (2016).
18. Sangiovanni, D. G., Chirita, V. & Hultman, L. Electronic mechanism for toughness enhancement in $Ti_xM_{1-x}N$ (M = Mo and W). *Phys. Rev. B* **81**, 104107 (2010).
19. Koutná, N. et al. Point-defect engineering of MoN/TaN superlattice films: a first-principles and experimental study. *Mater. Des.* **186**, 108211 (2020).
20. Koutná, N., Holec, D., Friák, M., Mayrhofer, P. H. & Šob, M. Stability and elasticity of metastable solid solutions and superlattices in the MoN–TaN system: First-principles calculations. *Mater. Des* **144**, 310–322 (2018).
21. Helmersson, U. et al. Growth of single-crystal TiN/VN strained-layer superlattices with extremely high mechanical hardness. *J. Appl. Phys.* **62**, 481–484 (1987).
22. Niu, H. et al. Extra-electron induced covalent strengthening and generalization of intrinsic ductile-to-brittle criterion. *Sci. Rep.* **2**, 718 (2012).
23. Hilliard, J. E. Estimating grain size by the intercept method. *Met. Prog* **85**, 99–102 (1964).
24. Gammer, C., Mangler, C., Rentenberger, C. & Karnthaler, H. P. Quantitative local profile analysis of nanomaterials by electron diffraction. *Scr. Mater* **63**, 312–315 (2010).
25. Klimashin, F. F., Koutná, N., Euchner, H., Holec, D. & Mayrhofer, P. H. The impact of nitrogen content and vacancies on structure and mechanical properties of Mo-N thin films. *J. Appl. Phys.* **120**, 185301 (2016).
26. Koutná, N., Holec, D., Svoboda, O., Klimashin, F. F. & Mayrhofer, P. H. Point defects stabilise cubic Mo-N and Ta-N. *J. Phys. D. Appl. Phys.* **49**, 375303 (2016).
27. Kutschej, K. et al. Structure, mechanical and tribological properties of sputtered $Ti_{1-x}Al_xN$ coatings with $0.5 \leq x \leq 0.75$. *Surf. Coat. Technol* **200**, 2358–2365 (2005).
28. PalDey, S. & Deevi, S. C. Single layer and multilayer wear resistant coatings of (Ti,Al)N: a review. *Mater. Sci. Eng. A* **342**, 58–79 (2003).
29. Chu, X. & Barnett, S. A. Model of superlattice yield stress and hardness enhancements. *J. Appl. Phys.* **77**, 4403–4411 (1995).
30. Chen, X., Du, Y. & Chung, Y. W. Commentary on using H/E and H 3 /E 2 as proxies for fracture toughness of hard coatings. *Thin Solid Films* **688**, 137265 (2019).
31. Koutná, N. et al. Correlating structural and mechanical properties of AlN/TiN superlattice films. *Scr. Mater.* **165**, 159–163 (2019).
32. Bielawski, M. & Chen, K. Computational evaluation of adhesion and mechanical properties of nanolayered erosion-resistant coatings for gas turbines. *J. Eng. Gas Turbines Power* **133**, 042102 (2010).
33. Muenz, W.-D. et al. Industrial scale manufactured superlattice hard PVD coatings. *Surf. Eng.* **17**, 15–27 (2001).
34. Petrov, I. et al. Ion-assisted growth of $Ti_{1-x}Al_xN/Ti_{1-y}Nb_yN$ multilayers by combined cathodic-arc/magnetron-sputter deposition. *Thin Solid Films* **302**, 179–192 (1997).
35. Buchinger, J. et al. Toughness enhancement in TiN/WN superlattice thin films. *Acta Mater.* **172**, 18–29 (2019).
36. Hovsepian, P. E. et al. Novel HIPIMS deposited nanostructured CrN/NbN coatings for environmental protection of steam turbine components. *J. Alloys Compd.* **746**, 583–593 (2018).
37. Schlögl, M., Kirchlechner, C., Paulitsch, J., Keckes, J. & Mayrhofer, P. H. Effects of structure and interfaces on fracture toughness of CrN/AlN multilayer coatings. *Scr. Mater.* **68**, 917–920 (2013).
38. Shinn, M. & Barnett, S. A. Effect of superlattice layer elastic moduli on hardness. *Appl. Phys. Lett.* **64**, 61–63 (1994).
39. Kresse, G. & Furthmüller, J. Efficiency of ab-initio total energy calculations for metals and semiconductors using a plane-wave basis set. *Comput. Mater. Sci.* **6**, 15–50 (1996).
40. Kresse, G. & Joubert, D. From ultrasoft pseudopotentials to the projector augmented-wave method. *Phys. Rev. B* **59**, 1758–1775 (1999).
41. Kohn, W. & Sham, L. Self-consistent equations including exchange and correlation effects. *Phys. Rev.* **140**, A1133 (1965).
42. Perdew, J. P., Burke, K. & Ernzerhof, M. Generalized gradient approximation made simple. *Phys. Rev. Lett.* **77**, 3865–3868 (1996).
43. Wei, S.-H., Ferreira, L. G., Bernard, J. E. & Zunger, A. Electronic properties of random alloys: Special quasirandom structures. *Phys. Rev. B* **42**, 9622–9649 (1990).
44. Birch, F. Finite elastic strain of cubic crystals. *Phys. Rev* **71**, 809–824 (1947).
45. Le Page, Y. & Saxe, P. Symmetry-general least-squares extraction of elastic data for strained materials from ab initio calculations of stress. *Phys. Rev. B* **65**, 1–14 (2002).
46. Le Page, Y. & Saxe, P. Symmetry-general least-squares extraction of elastic coefficients from ab initio total energy calculations. *Phys. Rev. B: Condens. Matter Mater. Phys* **63**, 1–8 (2001).
47. Yu, R., Zhu, J. & Ye, H. Q. Q. Calculations of single-crystal elastic constants made simple. *Comput. Phys. Commun.* **181**, 671–675 (2010).
48. Moakher, M. & Norris, A. N. The closest elastic tensor of arbitrary symmetry to an elasticity tensor of lower symmetry. *J. Elast.* **85**, 215–263 (2006).
49. Reuss, A. Berechnung der Fließgrenze von Mischkristallen auf Grund der Plastizitätsbedingung für Einkristalle. *ZAMM—Zeitschrift Angew. Math. Mech* **9**, 49–58 (1929).
50. Voigt, W. *Lehrbuch der Kristallphysik* (Vieweg+Teubner Verlag, 1928).
51. Nye, J. F. *Physical Properties of Crystals: Their Representation by Tensors and Matrices* (Oxford University Press, 1985).
52. Grimsditch, M. & Nizzoli, F. Effective elastic constants of superlattices of any symmetry. *Phys. Rev. B* **33**, 1–2 (1986).
53. Lazar, P., Redinger, J. & Podloucky, R. Density functional theory applied to V N / Ti N multilayers. *Phys. Rev. B* **76**, 174112 (2007).
54. Řehák, P., Černý, M. & Holec, D. Interface-induced electronic structure toughening of nitride superlattices. *Surf. Coat. Technol* **325**, 410–416 (2017).
55. Giannuzzi, L. A. & Stevie, F. A. A review of focused ion beam milling techniques for TEM specimen preparation. *Micron* **30**, 197–204 (1999).
56. Keckes, J. et al. X-ray nanodiffraction reveals strain and microstructure evolution in nanocrystalline thin films. *Scr. Mater* **67**, 748–751 (2012).
57. Fischer-Cripps, A. C. *Nanoindentation Testing* 21–37 (Springer, New York, NY, 2011).
58. Oliver, W. C. & Pharr, G. M. An improved technique for determining hardness and elastic modulus using load and displacement sensing indentation experiments. *J. Mater. Res.* **7**, 1564–1583 (1992).
59. Menčík, J., Munz, D., Quandt, E., Weppelmann, E. R. & Swain, M. V. Determination of elastic modulus of thin layers using nanoindentation. *J. Mater. Res.* **12**, 2475–2484 (1997).
60. Brinckmann, S., Matoy, K., Kirchlechner, C. & Dehm, G. On the influence of microcantilever pre-crack geometries on the apparent fracture toughness of brittle materials. *Acta Mater.* **136**, 281–287 (2017).
61. Matoy, K. et al. A comparative micro-cantilever study of the mechanical behavior of silicon based passivation films. *Thin Solid Films* **518**, 247–256 (2009).
62. Frantsevich, I. N., Voronov, F. F. & Bokuta, S. A. *Elastic Constants and Elastic Moduli of Metals and Insulators Handbook* (Naukova Dumka, 1983).
63. Pugh, S. F. XCII. Relations between the elastic moduli and the plastic properties of polycrystalline pure metals. *London, Edinburgh, Dublin Philos. Mag. J. Sci* **45**, 823–843 (1954).
64. Niu, H. et al. Extra-electron induced covalent strengthening and generalization of intrinsic ductile-to-brittle criterion. *Sci. Rep.* **2**, 718 (2012).

Acknowledgements

The authors acknowledge the financial support by the Austrian Federal Ministry of Economy, Family and Youth and the National Foundation for Research, Technology and Development. We also thank for the financial support of Plansee Composite Materials GmbH, and Oerlikon Surface Solutions AG. The computational results were achieved using the Vienna Scientific Cluster (VSC), X-ray diffraction studies were performed at the X-ray center of TU Wien (XRC), SEM, and TEM work was performed using facilities of the USTEM at TU Wien. We also thank the Institute for Mechanics of Materials and Structures of TU Wien for providing the PI85-SEM indenter. We further acknowledge the granted use of the Nanofocus Endstation of the Beamline P03 of PETRAIII at DESY, a member of the Helmholtz Association (HGF). NK acknowledges the DOC fellowship from the Austrian Academy of Sciences. The authors acknowledge TU Wien Bibliothek for financial support through its Open Access Funding Programme.

Author contributions

R.H., N.K., T.W., A.D., and C.K. and performed experiments and analyzed data. R.H., N.K., D.H., M.B., and P.H.M. wrote the manuscript. S.K. and P.H.M. developed the concept and managed the project.

Competing interests

The authors declare no competing interests.

Additional information

Supplementary information is available for this paper at https://doi.org/10.1038/s43246-020-00064-4.

Correspondence and requests for materials should be addressed to R.H.

Reprints and permission information is available at http://www.nature.com/reprints

Publisher's note Springer Nature remains neutral with regard to jurisdictional claims in published maps and institutional affiliations.